A CFD Benchmark for Flow Separation Control Application

V. Ciobaca[1], **J. Dandois**[2] **and H. Bieler**[3]
[1]DLR, Institute of Aerodynamics and Flow Technology, 38108 Braunschweig,
Germany. vlad.ciobaca@dlr.de
[2]ONERA, Applied Aerodynamics Department, 92160 Meudon,
France. julien.dandois@onera.fr
[3]Airbus Operations GmbH, Flight Physics - Aerodynamics,
28199 Bremen, Germany heribert.bieler@airbus.com

Received date: 2/25/2014; Accepted date: 9/29/2014

ABSTRACT

This paper describes numerical studies conducted for one promising active flow control (AFC) technology for high-lift configurations, namely the pulsed blowing through slots. The selected configuration is a 2D high-lift airfoil, known as DLR-F15, and represents the state of the art for transonic turbulent airfoil for modern civil transport aircraft. The slot-actuators are applied on the suction side of the trailing edge flap to prevent local flow separation. The studies are addressed to evaluate the feasibility of unsteady RANS simulations to reproduce the trends discovered in experiments. Within the European framework of JTI-Clean Sky, numerical and experimental studies for low speed AFC are addressed. In this project, a computational study was performed at ONERA and DLR for verifying their standard approaches for AFC with available time-averaged experimental data and performing a direct comparison of computed flow unsteadiness and its implications. The results for moderate angles of attack with and without control show that the numerical predictions are in good agreement with the experiment and in between each other provided that the laminar to turbulent boundary layer transition on the flap is considered.

1. INTRODUCTION

The suppression of flow separations by active flow control techniques is a promising technology for future transport aircraft [1]–[3]. Steep landing approaches and reduced system weights are of significant relevance for any novel high-lift design. It is expected that active separation control can lead to a significant reduction of the system complexity in the case of high-lift configurations.

In the past, the need for increasing lift of civil transport aircraft during landing was countered by increasing the complexity of the high-lift system, e.g. by employing multi-slotted instead of single-slotted flaps [4]. Recent research has proven active flow control by means of pulsed blowing through slots to be an alternative to realize the lift requirements. This AFC method forces the flow to stay attached to the trailing edge flap at deflection angles, at which the flow would separate without active intervention. Therefore this technique is promising to enable the design of high-lift systems of reduced mechanical complexity.

In the last decade, a variety of flow control studies have been addressed. Numerous investigations aimed at simple hinged trailing edge flaps while others tackled the improvement of high-lift configurations with slotted flaps. Representative studies for high-lift can be found in [5]–[10], without the scope of completeness.

Especially for active flap separation control through periodic excitation numerous experimental investigations were carried out in the past at Technical University Berlin (TUB). Such previous experiments [11]–[13] have shown encouraging results for trailing-edge flap separation suppression and lift gains of up $\Delta C_L = 0.6$ have been measured for a two-dimensional high-lift airfoil. Based on that, numerical studies [14] have been addressed to evaluate the feasibility of unsteady RANS simulations to reproduce the trends discovered in experiments.

By its physics, this AFC application is a complex unsteady phenomenon. However, many CFD approaches for AFC are poorly validated, mostly due to lack of available accurate measurements [15].

The unsteadiness is often triggered in the numerics by a transpiration boundary condition without modelling the complete actuation system. The boundary condition is then applied on the airfoil surface or on the bottom of a modelled portion of the actuation's slit. Such deviations may lead to discrepancies between different simulations tools.

Within the European framework of JTI-Clean Sky [17], a work package of the Smart Fixed Wing (SFWA) project addresses numerical and experimental studies for low speed AFC. This AFC technique is among others flow control studies focus for this project.

Within this framework, a computational study was performed at ONERA and DLR for verifying their standard approaches for AFC with available time-averaged experimental data and for performing a direct comparison of computed flow unsteadiness and its implications. The selected configuration is a 2D high-lift airfoil, known as DLR-F15, and represents the state of the art for transonic turbulent airfoil for modern civil transport aircraft, [16]. A wind tunnel test was performed in 2010 at Airbus' facility in Filton, F-LSWT, within the European project AVERT and with the support of Technical University Berlin and National Institute for Aerospace Research INCAS, Romania.

This paper presents the findings of the numerical investigations, where the solution of the Reynolds Averaged Navier Stokes (RANS) equations is carried out using the solvers ONERA-elsA- and, DLR-TAU-code, respectively.

In the followings the geometrical setup, the mesh generation and the numerical method are presented. Afterwards the results of the numerical studies are discussed including final conclusions.

2. THE HIGH-LIFT AIRFOIL DLR-F15

The geometry of interest is the two-dimensional DLR-F15 2-element high-lift airfoil (Figure 1), with a slatless (retracted slat) configuration [16]. The retracted (slat and flap) model chord is c = 600 mm The high-lift airfoil originates as a section of a 3D wing design for a research configuration of a single-aisle aircraft. This airfoil is used intensively for more than 7 years at DLR for high-lift investigations, e.g. flow control technologies, noise reduction techniques. The flight conditions for this airfoil section are a Mach number $M = 0.15$, and a Reynolds number $Re_c = 7 \times 10^6$ based on the design point of the 3D wing with the corresponding backwards transformation to the two-dimensional section.

The numerical investigations are using inflow conditions from existing low speed atmospheric tunnel tests. The Mach number M is equal to 0.15 and the Reynolds number based on the retracted chord length is $Re_c = 2 \times 10^6$ which correspond to the low speed atmospheric tunnel conditions at $U_\infty = 50$ m.s^{-1} and at the ambient temperature of $T \approx 293$ K. Since the model set-up in the wind tunnel is two-dimensional, numerical simulations are performed in 2D. The trailing edge flap is deflected according to the parameters shown in Table 1. This is the most receptive flap setup for AFC that was found during wind tunnel testing.

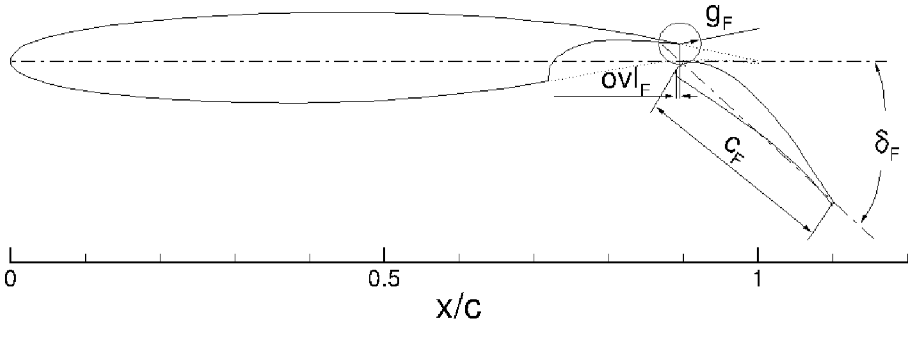

Figure 1. The DLR-F15 high-lift airfoil with the definition of parameters for the trailing-edge flap.

Table 1. Parameters of the trailing edge flap

Configuration	Flap gap, g_F [mm]	Flap chord, c_F [mm]	Flap deflection, δ_F [°]	Flap overlap, ovl_F [mm]
DLR-F15, 2eFC	15.919	168	45.01	3.303

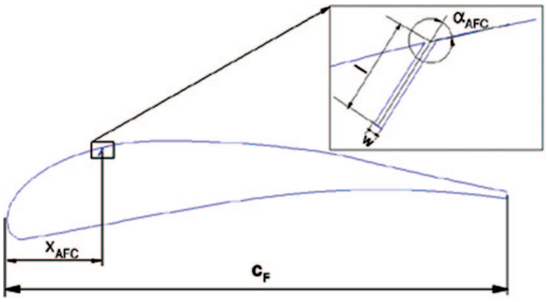

Figure 2. Schematic view of the slot-actuator positioning.

Table 2. Parameters of actuation slit

Configuration	**Width, w [mm]**	**Position, x_{AFC}/c_F [%]**	**Blowing direction, α_{AFC} [°]**	**Slit length, l [mm]**
DLR-F15, 2eFC	0.3	20	45	solver specific

2.1. The Active Flow Control System

The slot-actuators are applied on the suction side of the trailing edge flap to prevent local flow separation. The experimental actuation system consists of three major components: a pressurized air supply, fast switching solenoid valves to generate pulsed airflow, and actuator chambers. The jet enters the ambient flow through an orifice in the flap's surface as a fast, pulsed jet. All actuator slots have a constant width of 0.3 mm. The AFC slits which are included in the flap geometry are partially modelled in the numerical simulations. Figure 2 shows the slit geometry which has a constant cross section and is inclined downstream. The specifications of the actuation slit are depicted in Table 2.

2.2. Definition of Flow Control Parameters

The parameters used in relation with the active flow control application are the blowing momentum coefficient C_μ, the non-dimensional actuation frequency F^+ and the actuation duty cycle DC. The blowing momentum coefficient was first introduced by Poisson-Quinton [18] and for this application is defined as:

$$C_\mu = \frac{\frac{1}{DC} \times \dot{m}_{jet} \times u_{jet}}{\frac{1}{2} \times \rho_\infty \times U_\infty^2 \times A_{ref}} \tag{1}$$

where, at the fraction numerator, $\dot{m}_{jet}$ is the time-averaged actuation mass-flow and u_{jet} is the time-averaged jet velocity, and DC is the actuation duty cycle. The denominator of the fraction is the product of the dynamic pressure ($0.5\,\rho U^2$) and the airfoil reference area, A_{ref}.

The non-dimensional actuation frequency F^+ is defined as:

$$F^+ = \frac{f \times c_F}{U_\infty} \tag{2}$$

where f is the physical actuation frequency. For determining this variable the characteristic length is the flap chord length c_F, and the characteristic velocity is the reference inflow speed.

The actuation duty cycle DC shows the percentage of time in which the actuation valve remains open t_{open} relative to the actuation period T:

$$DC = \frac{t_{open}}{T} \tag{3}$$

3. THE MESH GENERATION

For the elsA computations a structured mesh with $2.7 \cdot 10^5$ grid points is investigated (Figure 3a), while for the TAU simulations a hybrid mesh with $3.7 \cdot 10^5$ nodes is used (Figure 3b).

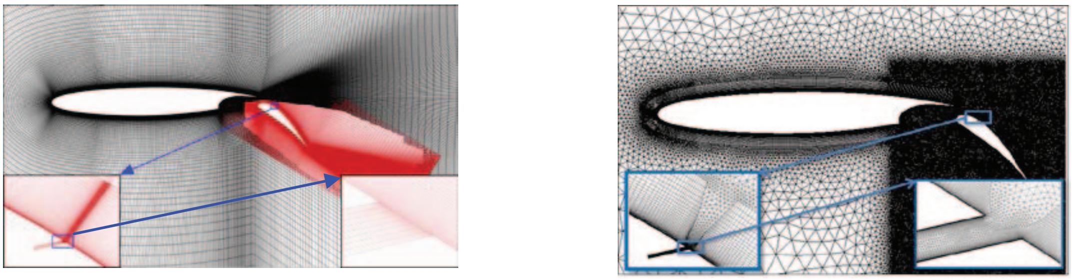

a) Structured grid used with ONERA-elsA b) Hybrid grid used with DLR-TAU

Figure 3. Spatial discretizations used for the AFC simulations.

The elsA structured mesh has been created using the ANSYS-ICEM Hexa software. The mesh has a C-type topology. As shown by Figure 3a, the overset grid method is used to add the flap mesh in the main body one. This method enables reduced meshing time for complex geometries without penalizing the quality of the results. The size of the first cell is chosen in order to insure $y^+ = 1$ at the wall. The flow inside the actuation slot is computed in order to have the correct velocity profile at the orifice exit. Lateral boundaries are treated under a noslip hypothesis, which allows for some boundary-layer developments inside the cavity. The slot width is discretized with 8 cells.

The hybrid grids for the unsteady numerical investigation with the TAU code are generated with the commercial mesh generation software CENTAUR [19], which is characterized by a fast and stable generation of the grids. The grids have an O-topology, where for the boundary layer approximation quasi structured cells are generated next to the model surfaces with small initial spacing and smooth growing away from the surface, while the rest of the simulation domain is filled with triangular elements. Figure 3b shows the generated mesh for the DLR-F15 high-lift airfoil used for the simulations of the active flow control application. The height of the structured layers is adjusted to capture the local boundary layer, and consequently a reduced height of the structured stacks corresponds to the flap. At trailing edges the height of the structured cells needs to be modified because of geometrical constrains. The number of stacks is reduced at the trailing edge in order to avoid the pullback of the structured cells too far upstream which are needed to assure a proper discretization for the local boundary layer. With the knowledge of a physical massive flap separation, the surroundings of the flap suction side have been discretized by tiny cells of constant spacing. The mesh contains $3.7 \cdot 10^5$ nodes. The mesh extends 100 c in all directions (two-dimensional) where the farfield boundary condition is imposed. A portion of the actuation slot is modelled that extends 20 w below the flap surface, where w is the slot width. The side-walls of the actuation slot are treated as viscous walls and the actuation boundary condition is applied at the slot bottom. Here, the slot bottom is discretized with about 70 nodes.

4. THE NUMERICAL METHOD

The solution of the Reynolds Averaged Navier Stokes (RANS) equations is carried out using the solvers ONERA-elsA- and, DLR-TAU-code, respectively.

elsA is a compressible structured, multiblock, cell-centred CFD software developed by ONERA [20], [21]. The Reynolds-averaged form of the Navier–Stokes equations is solved using Jameson's second-order central scheme with artificial viscosity for the spatial discretisation. The 2nd order dissipation term is equal to zero and the 4th order dissipation coefficient is equal to 0.016. For turbulent equations, a Roe scheme coupled with Harten's correction has been used (Harten coefficient equal to 0.01). The implicit phase is solved using a lower-upper symmetric successive overrelaxation technique, and convergence is accelerated through a two levels, v-cycle, multigrid algorithm. Steady-state solutions are obtained using a quasi-stationary backward-Euler integration with a CFL number equal to 50. Turbulence closure is achieved using the one-equation model of Spalart and Allmaras [22] (SA).

TAU is a finite volume compressible solver developed at DLR [23]. A second order central scheme is used for the discretization of the convective fluxes. The artificial dissipation based upon the original settings of Jameson is applied with a 2nd order dissipation term of 1/2, and a 4th order dissipation coefficient of 1/64. The chosen approach for the time integration is a semi-implicit LUSGS time

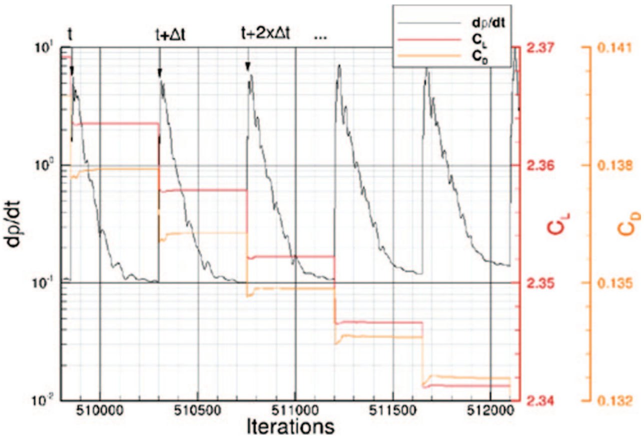

Figure 4. DLR-TAU: convergence plot for density residual and aerodynamic coefficients: lift and drag.

integration method using a CFL number of 5. In addition a point explicit residual smoother is used for convergence acceleration. Concerning the turbulence modeling, the advanced Shear Stress Transport model (SST) from Menter [24] is used. For this two equation model a different than standard wall limiter type for the ω-equation is used, where the lower bound of ω is limited based on experimental assumptions for the wall roughness [25]. This limiter previously showed good and stable results for cases with high complexity.

The URANS simulations are conducted for both solvers with a dual time stepping approach. Dual time is an alternative means for computations of unsteady flow problems. The time derivate of the considered governing equations is discretized with backward difference formulae, and the resulting algebraic system is solved by iterating to a steady state in an artificially introduced pseudo time. The inner iteration strongly resembles the iteration for convergence to steady state, so that the techniques applied for efficient steady state convergence may be applied. The choice of the time step size and the number of inner iterations is framework dependent. With the DLR-TAU code 100 physical time steps Δt, are used for each actuation cycle, and up to 500 inner iterations are required for the local convergence within one time step (Figure 4). With the ONERA-elsA solver the simulation of one actuation cycle is time-discretized by 800 physical time steps, where 200 iterations are utilized for the convergence in each inner loop.

Here, the simulations are conducted with the assumptions of a fully turbulent main wing and a transition free trailing-edge flap. The experimental model had a transition fixing device at wing leading edge and was transition free for the flap.

4.1. Transition Prediction

In order to estimate the boundary layer laminar turbulent transition the solvers make use of so-called transition prediction modules.

Transition-prediction capability has been introduced into the elsA code [26], based on application of criteria that were developed at ONERA for use in boundary-layer codes, such as bypass, TS and crossflow transition, and laminar-separation-bubble predictions. Those considered relevant here are, namely, the Arnal–Habiballah–Delcourt criterion for TS instabilities and the Gleyzes–Habiballah criterion for 2-D short bubble transition. The upstream turbulence rate and the turbulence rate outside the boundary layer have been set to 0.5%. The transition module is called at each time step.

For the TAU-solver the automatic transition prediction tool implemented by Krumbein and Krimmelbein [27]–[28] is used with a laminar-boundary layer code and a linear stability code coupled with the flow solver. The transition prediction approach is based on the e^N-method and since it is used for two-dimensional investigations it covers only the transition due to Tollmien-Schlichting (TS) instabilities. Because the pulsed blowing is a time-dependent phenomenon, the transition location becomes time-dependent, too. Here, the transition prediction is carried on each tenth physical time-step.

4.2. The Actuation Boundary Condition

The actuation boundary condition, at the actuator-slot's bottom, is of particular interest. Therefore the next subsections present the used numerical boundary conditions.

4.2.1. The Approach with the TAU-code

For a non-reflecting inflow boundary condition of three-dimensional subsonic flow, according to theory, four quantities need to be specified by boundary values and the fifth quantity is taken from the solution inside the flow domain. Within TAU, the conservative variables like density and momentum are prescribed and the pressure is extrapolated from the solution inside the domain [29]. Therefore, the maximum jet velocity, the actuation direction and the jet density are user specified variables, where the jet density remains constant for the dynamic actuation process. Finally, for the description of the turbulence terms at the actuation boundary a method is utilized which uses an empirical relation for the eddy viscosity from experimental data for round and plane jets. For the two equation model of Menter SST k-ω, the turbulent kinetic energy k and specific dissipation rate ω are stipulated in relation with the jet turbulent intensity.

This approach for AFC simulations was previously applied for single actuators on a zero-pressure gradient flat plate [30] and for a slot-actuator on a trailing edge flap of 2D high-lift airfoils [14] as part of the verification and validation process. Here, for the pulsed blowing application the jet velocity changes over time with a square shape signal (Figure 5). The jet velocity at the inflow boundary condition is defined as:

$$u_{jet}(t) = u_{jet,\max} \times I(t - t_{offset}) \tag{7}$$

where

$$\begin{aligned} I(t) &= 1 \text{ for } t \in [0; T_h] \\ &= 0 \text{ for } t \in [T_h; T_f] \end{aligned} \tag{8}$$

where t_{offset} is time delay which can be varied, T_f is the actuation period, T_h is the opening time of the valve and T_l is the closed time.

In order to avoid a sharp jump from 0 to 1, a smoothing method is applied. A time is introduced over which u_{jet} is increased from 0 to its maximum value. The user defined time for smoothing the pulsed signal is typically two orders of magnitudes lower than the actuation period. The modelling of parts of the actuator-slots is considered a necessity, where the formulation of the inflow boundary condition ensures an accurate mass flow. Moreover, the inclusion of actuator-slits is the only possibility to ensure a correct outflow direction and velocity profile.

4.2.2. The Approach with the elsA-code

Like in the TAU code, since it is a subsonic inflow boundary condition, four quantities need to be specified by the user and the fifth condition is taken from the solution inside the flow domain. In the elsA software, the mass flow rate, the stagnation enthalpy and the flow direction are user specified variables. Turbulent variables are also imposed by the user in order to match the desired turbulence level.

Also like in the TAU code, a square shape signal is used for the mass flow rate with a first order low-pass filter which response time can be changed by the user (see Figure 6). Here, the response time is chosen equal to 0.5ms. The frequency and the duty cycle are also parameters. Moreover, a phase shift can be introduced in the case of several slots.

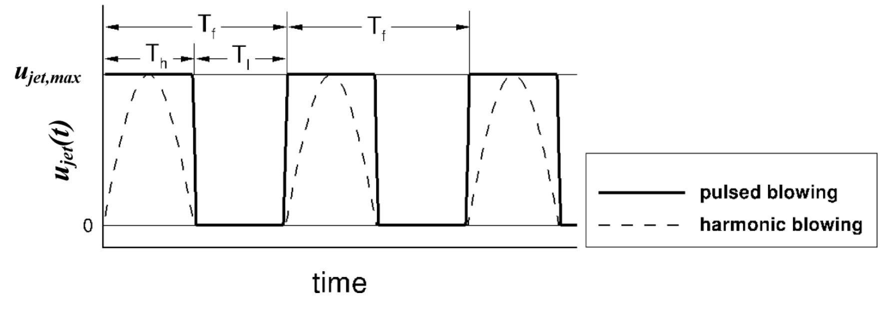

Figure 5. Schematic view of the pulsed blowing actuation.

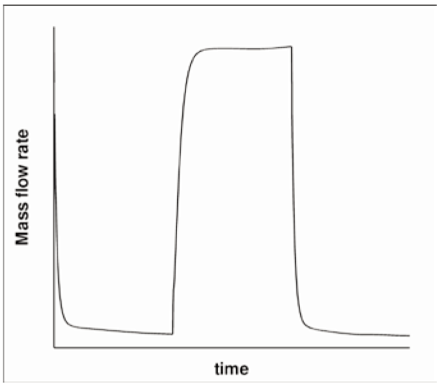

Figure 6. Schematic view of the pulsed blowing actuation.

5. RESULTS

In this section the results of the simulations with the TAU- and elsA-code are discussed and a comparison with experimental findings is depicted when appropriate. First, the time averaged aerodynamic coefficients and the time-averaged pressure distributions are presented. Afterwards, flow unsteady characteristics are shown for discussing the similarities and differences of the two numerical approaches for active flow control.

5.1. Time-averaged Aerodynamic Coefficients

Figure 7 and Figure 8 show the aerodynamic lift coefficients over the angle of attack for the baseline flow and for the momentum coefficient $C_\mu = 0.45\%$. The large difference between the experimental and numerical results can be explained by the fact that the experimental data are not wall-corrected. This is an aerodynamic problem related with measurements for two-dimensional airfoil models of

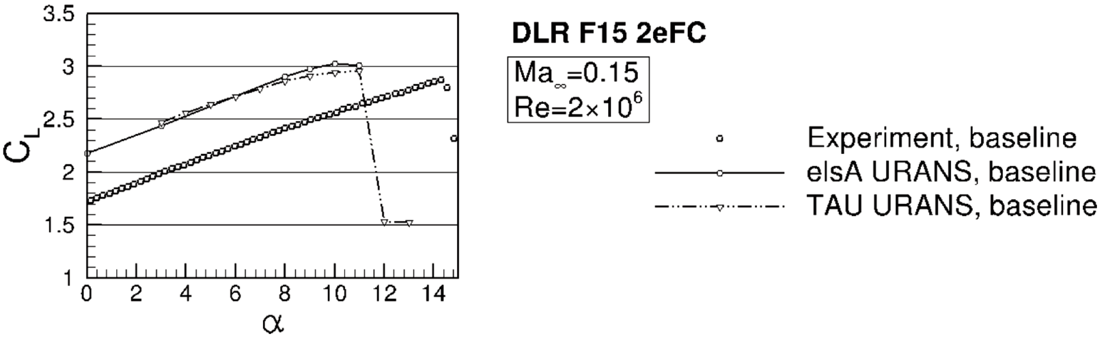

Figure 7. Time-averaged lift coefficients in comparison of CFD results with experimental findings for the *baseline* configuration.

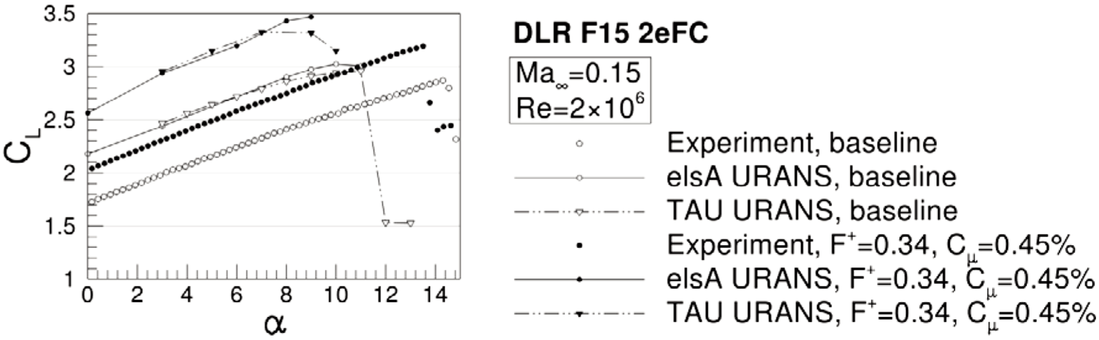

Figure 8. Time-averaged lift coefficients in comparison of CFD results with experimental findings for the baseline and with AFC.

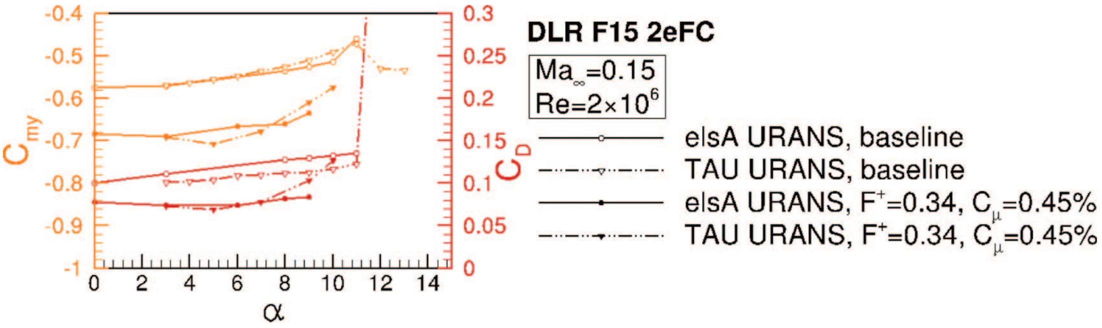

Figure 9. Time-averaged drag and pitching momentum coefficients from CFD results for the baseline and with AFC.

small aspect ratio that are mounted between small sideplates in classical wind tunnel test sections [31]. When high lift is generated at model mid-section the inflow angle of attack is largely disrupted compared with the geometrical angle of attack. The classical tunnel corrections cannot take account of these effects. Therefore, the drag and pitching momentum coefficients are not depicted for the experiment as they are faulty by far. In addition to the effect of the small aspect ratio of the model, there are a blockage effect due to the tunnel walls as well as significant three-dimensional effects due to the presence of side-plates and model-struts. Nevertheless, the lift enhancement through active flow control is noticeable in experiment and simulation, and the absolute lift increment is for the linear lift curve regime of $\Delta C_{L,\,CFD}$ = 0.5 and of $\Delta C_{L,\,EXP}$ = 0.3, respectively. Moreover, both approaches show an increase in maximum lift while the $\alpha_{CL,max}$ decreases for the AFC application in comparison with the corresponding baseline. The experimental study was successful for showing the positive AFC effect. The lift coefficient just points out that the measured trends in the wind-tunnel are correctly reproduced with both numerical methods. Moreover, the two numerical methods are in good agreement for the baseline flow as well as for the active flow control test case. The only distinguishable difference for the two numerical approaches with AFC is for the maximum lift. With the TAU code the maximum lift is reached at $\alpha = 8°$, followed by a smooth decrease in lift according to a trailing edge stall. The elsA results show a further linear increase in lift up to $\alpha = 9°$ which corresponds to the stall angle.

Additionally, the simulation shows a reduction of drag and an increase of pitch-down behaviour when flow control is active (Figure 9). The trends are consistent between the discussed numerical methods. The drag reduction by AFC is $\Delta C_{D,\,TAU} \approx 0.03$ and $\Delta C_{D,\,elsA} \approx 0.035$, respectively. The approach used with the DLR-TAU code depicts a lower drag coefficient for the baseline flow compared to the elsA results. The computed increase of the negative pitching momentum coefficient is $\Delta C_{my,\,TAU} \approx \Delta C_{my,\,elsA} \approx 0.12$.

5.2. Time-averaged Pressure Coefficients

Because of the model blockage effect, the comparison of pressure distribution in mid-section between experiment and simulation have to be performed at different angles of attack. Figure 10 and Figure 11 show the pressure distributions for the computed angle of attack $\alpha = 3°$. The angle of attack for the experiment ($\alpha = 7°$) is chosen in order to match the C_p peak at the main body leading edge between CFD results and experimental data. This means that there is an angle of attack correction of 4° (at $\alpha = 7°$) to correct the blockage and small aspect ratio model effects and retrieve the two-dimensional numerical simulation results which are performed without walls. Once this correction applied, the time-averaged flap loading and the corresponding changes with AFC are in good agreement between experiment and simulation for both numerical approaches. If the laminar to turbulent boundary layer transition had not been computed on the flap, the C_p peak at the flap leading edge would have been underestimated. The baseline flow separation above the flap surface is made evident in the experiment and the simulation through the pressure plateau on the flap suction side. Through the time-dependent pulsed blowing actuation the separation is suppressed as the pressure plateau vanishes and the flap suction peak is increased by $\Delta C_p \approx -1$ (as the pressure peak is decreased from $C_p \approx -3$ to $C_p \approx -4$). The air velocity at the main wing trailing edge is consequently increased and the local pressure coefficient decreases with $\Delta C_p \approx -0.5$. The pressure changes for the trailing edge flap are independent of angle of attack as long

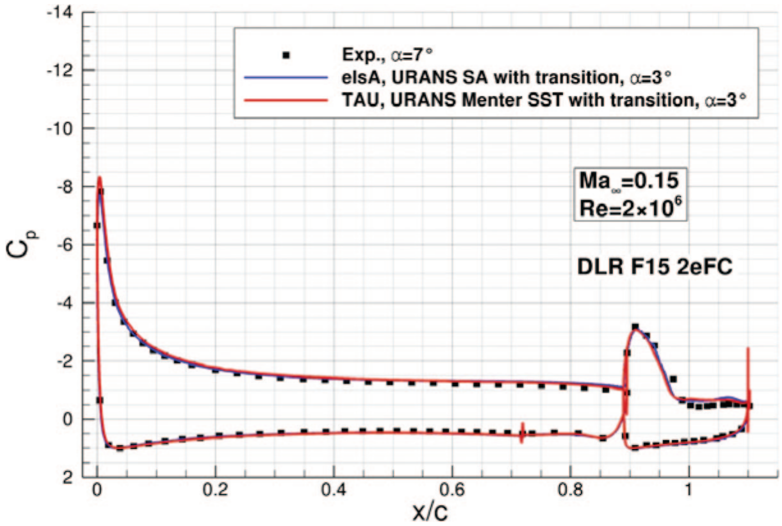

Figure 10. Time-averaged pressure distributions for a moderate angle of attack; comparison of CFD results with experimental findings for the *baseline* configuration.

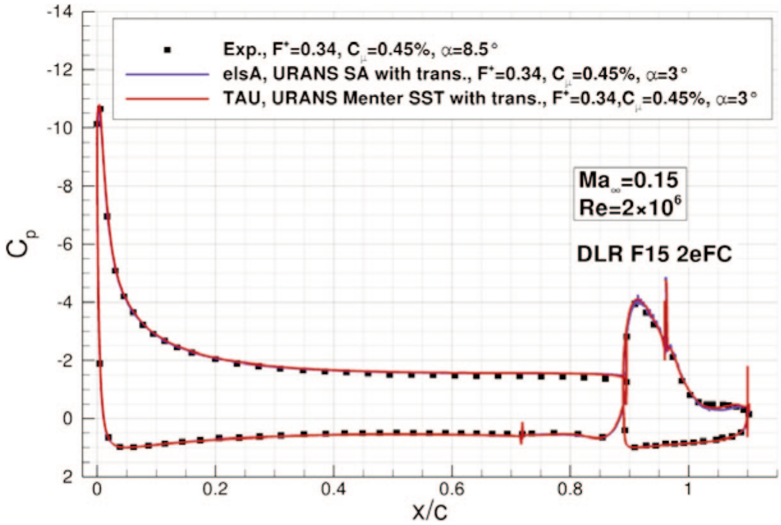

Figure 11. Time-averaged pressure distributions for a moderate angle of attack; comparison of CFD results with experimental findings *with AFC*.

as we do not leave the linear lift curve regime. Therefore, this exercise validates the time-averaged numerical findings for the baseline flow with massive separation and for a large blowing momentum coefficient with large airfoil lift enhancement and separation suppression.

Figure 12 and Figure 13 show the pressure distributions for the maximum angle of attack $\alpha_{CL,\,max}$. The two numerical methods show for the baseline flow a reduction of the flap suction peak compared to the moderate angle of attack. The wing $C_{p,\,min}$ stays below the critical pressure coefficient. With the further increase of angle of attack, a leading edge stall occurs as known from other data. The numerical results are in good agreement with each other and with the measurements. The pressure distributions with flow control (Figure 13) just underline the previous observations.

5.3. Flow Topologies

A comparison of the Mach field between elsA and TAU with the streamlines showing the separation size is displayed Figure 14. The separation bubble topology is very similar. The velocity deficit in the wake of the flap separation is larger in the TAU field than in the elsA one. Nevertheless, without detailed wind tunnel data, it is difficult to conclude definitely on this difference.

Figure 15 shows a comparison of the Mach fields with AFC on at $\alpha = 3°$ with the streamlines

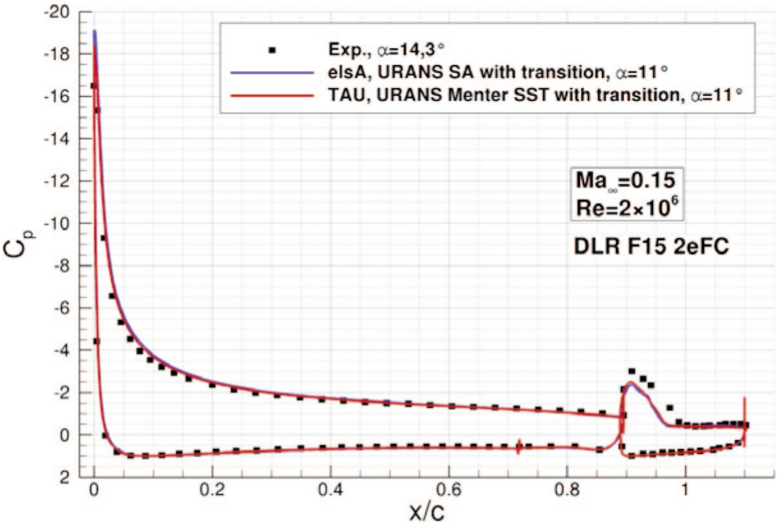

Figure 12. Time-averaged pressure distributions for $\alpha_{CL,\ max}$, comparison of CFD results with experimental findings for the *baseline* configuration.

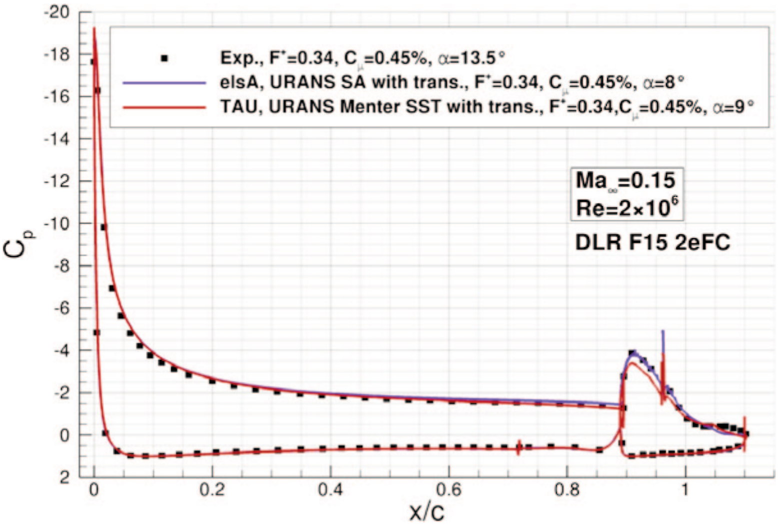

Figure 13. Time-averaged pressure distributions for $\alpha_{CL,\ max}$, comparison of CFD results with experimental findings *with AFC*.

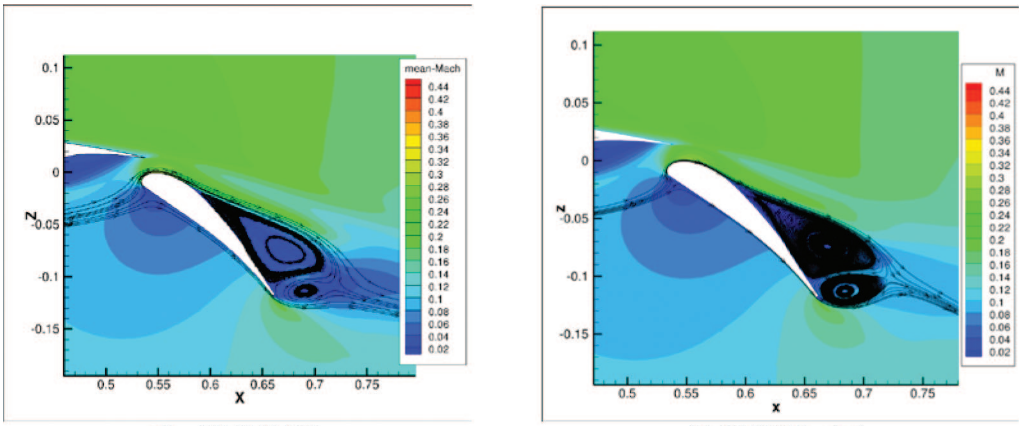

a) DLR-TAU b) ONERA-elsA

Figure 14. Time-averaged Mach number flowfields for a moderate angle of attack without AFC.

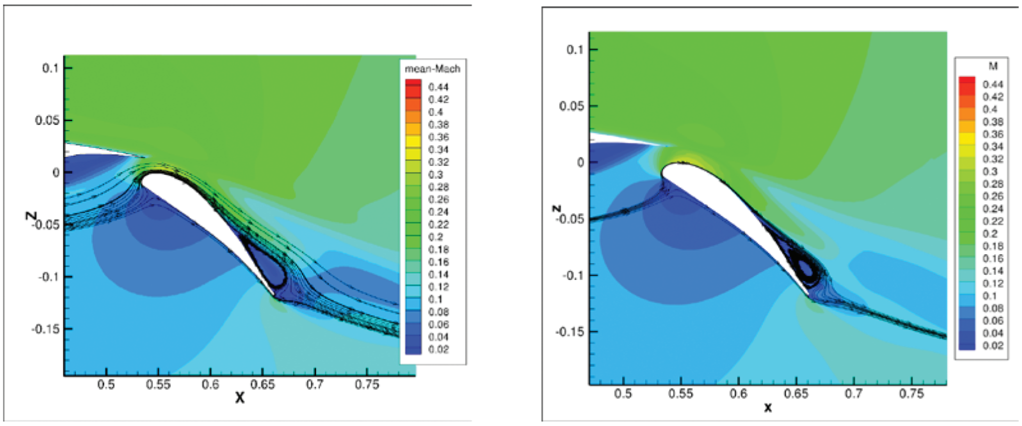

a) DLR-TAU b) ONERA-elsA

Figure 15. Time-averaged Mach-number flowfields for a moderate angle of attack with AFC.

between elsA and TAU. Once again, the flow topology and the size of the remaining separation are very similar. The velocity deficit in the wake of the flap is like in Figure 14 for the uncontrolled case larger in the TAU field than in the elsA one. Again, without detailed wind tunnel data, it is difficult to conclude definitely on this difference. By comparing Figure 14 and Figure 15, one can see the effect of pulsed blowing on the time-averaged separation bubble: the separation point has been delayed and the separation size has decreased but is not completely suppressed.

5.4 Flow Unsteady Characteristics

A comparison of the lift and drag evolution versus time for elsA and TAU at $\alpha = 3°$ is displayed in Figure 16. The simulations are conducted with active flow control at $C_\mu = 0.45\%$. The time dependent aerodynamic coefficients show that the maximum lift and maximum drag correspond to the end of the actuation-off stage ($U_{jet} = 0$) with the elsA solver, and close after beginning of the actuation-on stage ($U_{jet} = U_{jet,max}$) with the TAU code, respectively. Also, the results show that the minimum drag and minimum lift correspond to the end of the actuation-on stage ($U_{jet} = U_{jet,max}$). The numerical findings agree well with each other for mean, maximum and minimum values of the aerodynamic coefficients (see also Table 3). However, slight deviations are noticed close after the actuation is switched on and when the actuation is switched off. Most likely, these differences are caused by selected time resolutions for the simulations and by different switching signal blending functions at the boundary condition.

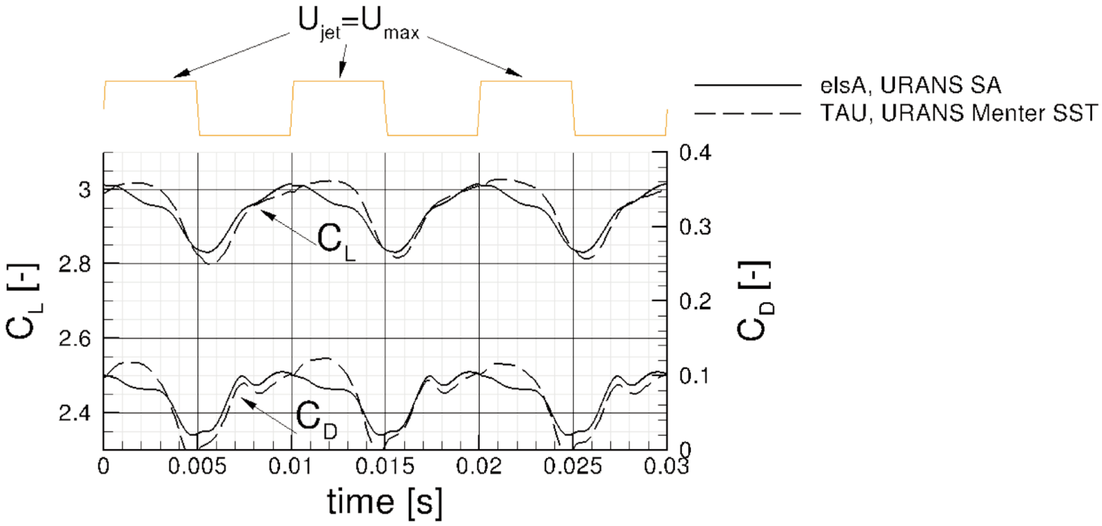

Figure 16. Lift and drag coefficient over time (α=3°).

Table 3. Time characteristics for the lift coefficient

Solver	Mean	Max	Min	RMS
elsA	2.94	3.01	2.83	0.065
TAU	2.95	3.02	2.80	0.072

Figure 17 and Figure 18 show the Mach fields for four distinct moments of the actuation period: beginning, mid-time and end of the blowing phase, and mid of the AFC-off phase. The lift is maximum at the beginning of the blowing and minimum at the end of the blowing. The effect of the pulsed blowing slot can be decomposed in four phases:

- At the beginning of the blowing phase (Fig. 17a and 18a), there is a small separation which extends over nearly one half the flap chord.
- During the blowing phase (Fig. 17b and 18b), this separation bubble grows in size. Its length is nearly constant but its thickness increases. This is due to the fact that the slot is not tangential but inclined at 45° with respect to the local tangent. The two slots have a different effect: with a tangential slot, the lift would increase during the blowing phase because of the added momentum in the boundary layer, the separation would be delayed farther downstream, it is more a "momentum effect"; with a slot inclined at 45°, the separation bubble size increases during the blowing phase so the lift decreases, it is more a "vortex effect".
- At the end of the blowing phase (Fig. 17c and 18c), the separation bubble detaches from the flap and is convected downstream. The lift is at this moment minimum. Two vortices are shade: first, a clockwise vortex then a counter-clockwise vortex.

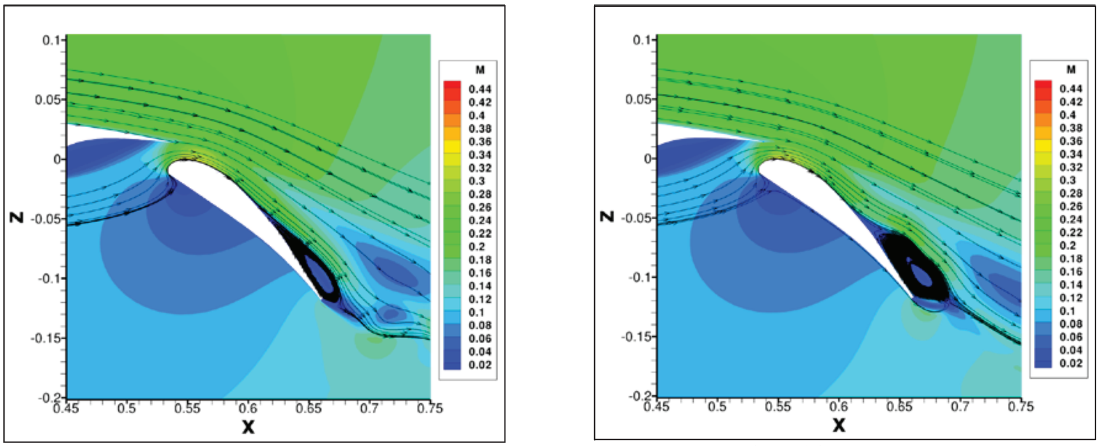

a) Beginning of AFC on

b) Mid of AFC on

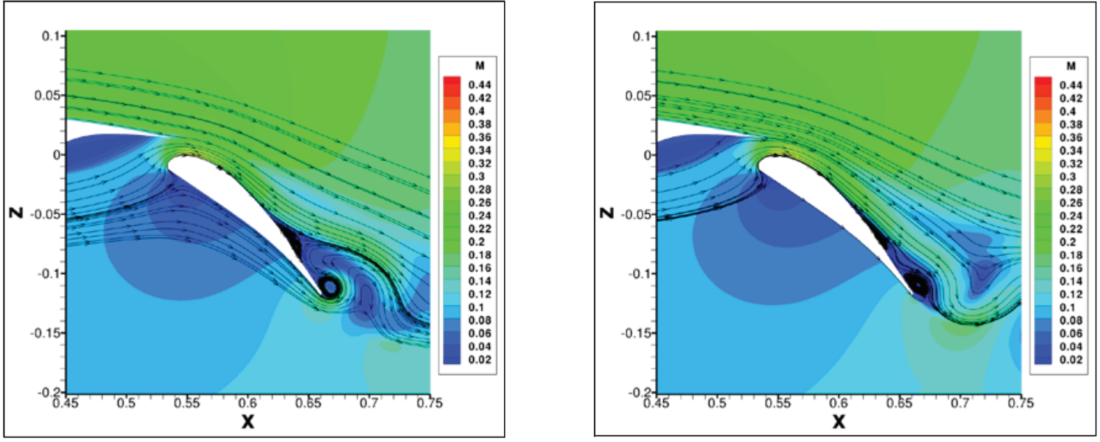

c) Beginning of AFC off

d) Mid of AFC off

Figure 17. Mach field for four snapshots of the actuation period (elsA).

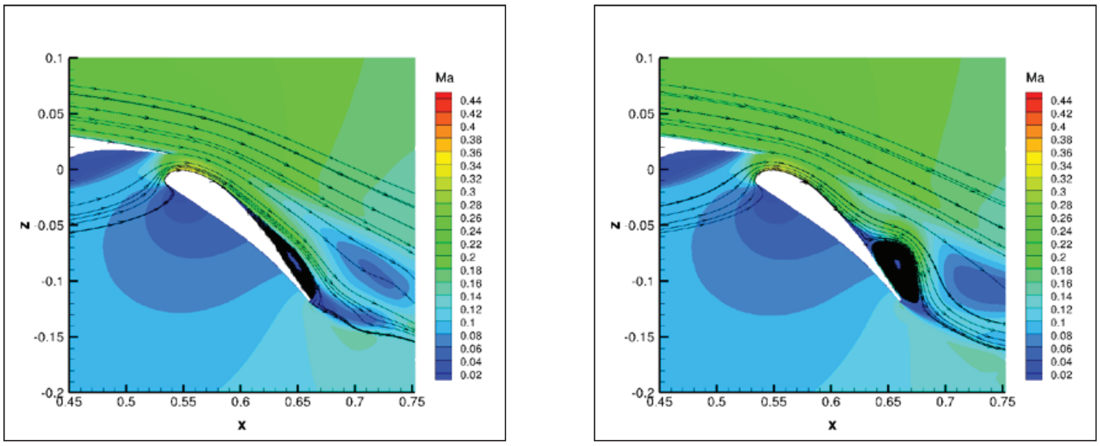

a) Beginning of AFC on

b) Mid of AFC on

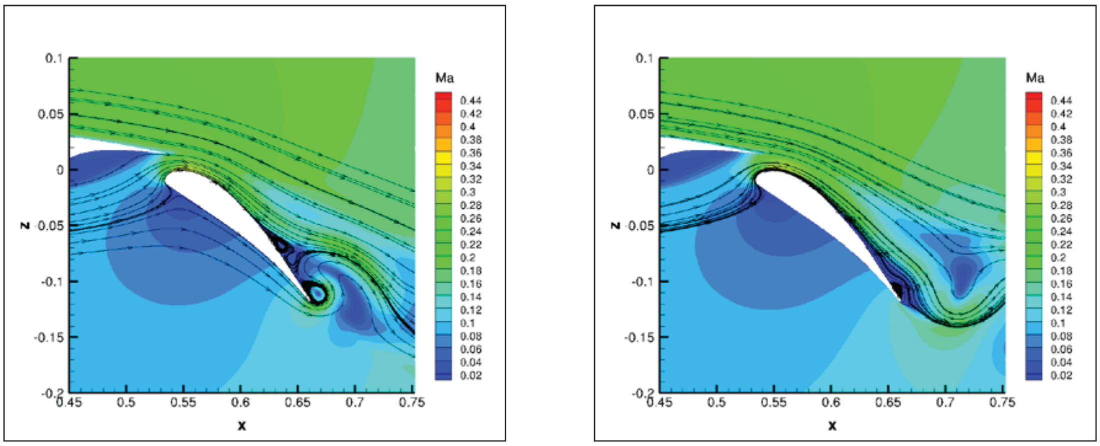

c) Beginning of AFC off

d) Mid of AFC off

Figure 18. Mach field for four snapshots of the actuation period (TAU).

- During the no-blowing phase (Fig. 17d and 18d), the counter-clockwise vortex induces a negative vertical velocity at the flap trailing edge which increases its effective camber and leads to an increase of the flap lift. The separation bubble height is also the smallest at this moment. Both effects result in a lift which is maximum at the end of the non-blowing phase.

As a result, the lift is maximum at the beginning of the blowing phase and by computing the correlation between the forcing signal and lift, a phase of 3π/2 (or –π/2) is found. The time-dependent flow topologies are in good agreement between the two approaches considering the position of the vortices rolling downstream as well as for the magnitude of the local Mach number.

6. CONCLUSIONS

A numerical benchmark with and without flow control on the unswept slat-less DLR-F15 turbulent airfoil at $M = 0.15$, and $Re_c = 2 \times 10^6$ has been conducted to compare ONERA and DLR best practices in the case of active flow control simulations.

Because the flow is separated on the flap, URANS computations with transition computation are necessary to obtain the same wall pressure distribution than the experimental data for the baseline. This transition on the flap has to considered in order to retrieve the right wall pressure distribution. The agreement between the elsA and TAU results is very good on the wall pressure distributions in the uncontrolled as well as in the controlled case. Despite the fact that different turbulence model, different meshes and time steps per period of actuation are used, the agreement is good. The only small differences between the two codes arise near $C_{L,max}$. Some slight differences have been observed in the Mach fields but without more detailed data, it was not possible to conclude. The flow topology for the baseline and the controlled case are very similar between the elsA and TAU results.

The time-dependent CFD results are very consistent and prove that the ONERA and DLR URANS – AFC best practices can further support the development of active flow control technologies.

7. AKNOWLEDGEMENT

The research leading to these results has received funding from the European Union's Seventh Framework Programme (FP7/2007-2013) for the Clean Sky Joint Technology Initiative under grant agreement number CSJU-GAM-SFWA-2008-001.

REFERENCES

[1] Gad-el Hak, M., *Flow Control: Passive, Active, Reactive Flow Management*, Cambridge University Press, New York, 2000.

[2] Greenblatt, D. and Wygnanski, I., The control of flow separation by periodic excitation, *Progress in Aerospace Sciences*, Vol. 36, No. 7, 2000, pp. 487–545.

[3] McLean, J.D., Crouch, J.D., Stoner, R.C., Sakurai, S., Seidel, G.E., Feifel, W.M., and Rush, H.M., *Study of the Application of Separation Control by Unsteady Excitation to Civil Transport Aircraft*, NASA/CR-1999–209338, 1999.

[4] Rudolph, P.K.C., High-Lift Systems on Commercial Subsonic Airliners, NASA CR 4746, Sept. 1996.

[5] Hassan, A.A., Improving Flap Aerodynamics Using Oscillatory Jet Control, AIAA Paper 2003–3664.

[6] Kiedaisch J., Nagib, H., and Demanett, B., Active Flow Control Applied to High-Lift Airfoils Utilizing Simple Flaps, AIAA Paper 2006–2856, 2006.

[7] Meunier, M., Simulation and Optimization of Flow Control Strategies for Novel High-Lift Configurations, *AIAA Journal*, Vol. 47, No. 5, 2009, pp. 1145–1157.

[8] Crowther, W. J., Separation Control on a Trailing-Edge Flap Using Air Jet Vortex Generators, *Journal of Aircraft*, Vol. 43, No. 5, 2006, 1589–1593.

[9] Khodadoust A., Washburn A, Active Control of Flow Separation on a High-Lift System with Slotted Flap at High Reynolds Number, AIAA Paper 2007–4424, 2007.

[10] Shmilovich, A. and Yadlin, Y., Active flow control for practical high-lift systems, *Journal of Aircraft*, Vol. 46, No. 4, 2009, pp.1354–1364.

[11] Petz, R. and Nitsche W., Active Separation Control on the Flap of a Two-Dimensional Generic High-Lift Configuration, *Journal of Aircraft* , Vol. 44, No. 3, 2007, pp. 865–874.

[12] Wild, J., Wichmann, G., Haucke, F., Peltzer, I. and Scholz, P., Large scale separation flow control experiments within the German Flow Control Network, AIAA Paper 2009–530, Jan. 2009.

[13] Haucke, F. and Nitsche, W., Active Flow Control on the Flap of a 2D High-Lift Wing Section at $Re = 1 \times 10^6$, AIAA Paper 2011–3359, June 2011.

[14] Ciobaca, V., Parameter study for a slatless 2D high-lift airfoil with active separation control using a URANS approach, *Notes on Numerical Fluid Mechanics and Multidisciplinary Design,* Vol. 121, pp. 135–142, 2012.

[15] Joslin, R.D., Miller, D.N., *Fundamentals and Applications of Modern Active Flow Control*, AIAA Book, Progress in Astronautics and Aeronautics, vol. 231, ISBN 978-1-56347-983-0, 2009.

[16] Wild, J., Experimental investigations of Mach- and Reynolds-number dependencies of the stall behavior of 2-element and 3-element high-lift wing sections, AIAA Paper 2012–108, 2012.

[17] http://www.cleansky.eu/

[18] Poisson-Quinton, Ph., Recherches théoriques et expérimentales sur le contrôle de couche limite, 7th Congress of Applied Mechanics, London, September 1948.

[19] http://centaursoft.com, May 2010.

[20] Cambier, L. and Gazaix, M., elsA: an Efficient Object-Oriented Solution to CFD Complexity, AIAA 2002–0108, 40th AIAA Aerospace Sciences Meeting & Exhibit, Reno (NV), January 14–17, 2002. http://elsa.onera.fr/

[21] Cambier, L. and Veuillot, J.-P., Status of the elsA CFD Software for Flow Simulation and Multidisciplinary Applications, AIAA 2008–0664, Jan. 2008.

[22] Spalart, P. and Allmaras, S., A One Equation Turbulence Model for Aerodynamic Flows, La Recherche Aérospatiale, 1994, Pages 5–21.

[23] Gerhold, T.: Overview of the Hybrid RANS Code TAU, *Notes on Numerical Fluid Mechanics and Multidisciplinary Design*, Vol. 89, Springer Verlag, pp. 81–92, 2005.

[24] Menter, F.R., Two-Equation Eddy-Viscosity Turbulence Models for Engineering Applications, *AIAA Journal*, Vol. 32, No. 8, 1994, pp. 1598–1605.

[25] Rudnik, R., Evaluation of the Performance of Two-Equation Turbulence Models for Airfoil Flows, Ph.D. Dissertation, Transportation and Applied Mechanics Dept., Technical University Berlin, Germany, 1997.

[26] Moens, F., Perraud, J., Séraudie, A. and Houdeville, R., Transition Measurement and Prediction on a Generic High-Lift Swept Wing, Proceedings of the Institution of Mechanical Engineers, Part G (*Journal of Aerospace Engineering*), Vol. 220, pp. 589–603, June 2006.

[27] Krumbein, A., Krimmelbein, N. and Schrauf G., Automatic transition prediction in a hybrid flow solver, part 1: Methodology and sensitivities, *Journal of Aircraft*, Vol. 46, No. 4, pp. 1176–1190, 2006.

[28] Krumbein, A., Krimmelbein, N. and Seyfert, C., Automatic transition prediction in unsteady airfoil flows using an unstructured CFD code, AIAA Paper 2011–3365, 2011.

[29] Knopp, T., The actuation boundary condition for flow control in the DLR TAU Code, DLR Report, IB-Nr. 224 – 2010 A44, Germany, 2010.

[30] Togiti, V., Ciobaca, V., Eisfeld, B. and Knopp T., Numerical Simulation of Steady Blowing Active Flow Control Using a Differential Reynolds Stress Model, *Proceedings of CEAS/KATnet II Conference on Key Aerodynamics Technologies*, Bremen, Germany, May 2009.

[31] Schlichting, H. and Truckenbrodt, E., *Aerodynamics of the Airplane*, McGraw-Hill, 1979.